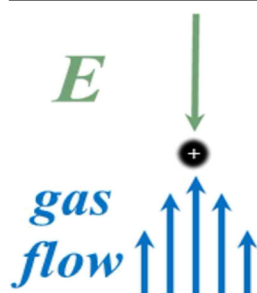


RESEARCH ARTICLE

Fundamentals of Trapped Ion Mobility Spectrometry Part II: Fluid Dynamics

Joshua A. Silveira, Karsten Michelmann, Mark E. Ridgeway, Melvin A. Park

Bruker Daltonics, 40 Manning Road, Billerica, MA 01821, USA



Abstract. Trapped ion mobility spectrometry (TIMS) is a new high resolution (R up to ~ 300) separation technique that utilizes an electric field to hold ions stationary against a moving gas. Recently, an analytical model for TIMS was derived and, in part, experimentally verified. A central, but not yet fully explored, component of the model involves the fluid dynamics at work. The present study characterizes the fluid dynamics in TIMS using simulations and ion mobility experiments. Results indicate that subsonic laminar flow develops in the analyzer, with pressure-dependent gas velocities between ~ 120 and 170 m/s measured at the position of ion elution. One of the key philosophical questions addressed is: how can mobility be measured in a dynamic system wherein the gas is expanding and its velocity is changing? We

noted previously that the analytically useful work is primarily done on ions as they traverse the electric field gradient plateau in the analyzer. In the present work, we show that the position-dependent change in gas velocity on the plateau is balanced by a change in pressure and temperature, ultimately resulting in near position-independent drag force. That the drag force, and related variables, are nearly constant allows for the use of relatively simple equations to describe TIMS behavior. Nonetheless, we derive a more comprehensive model, which accounts for the spatial dependence of the flow variables. Experimental resolving power trends were found to be in close agreement with the theoretical dependence of the drag force, thus validating another principal component of TIMS theory.

Keywords: Ion mobility mass spectrometry, Quadrupole time of flight mass spectrometry, TIMS theory, Resolving power, Gas flow

Received: 29 September 2015/Revised: 2 November 2015/Accepted: 6 November 2015/Published Online: 10 February 2016

Introduction

Conventional drift tube ion mobility spectrometry (IMS) involves the separation and characterization of ions on the basis of their transport through an effectively stationary gas in a uniform electric field. In the past few decades, several advances coupling drift tube IMS and other time-dispersive methods (i.e., traveling wave IMS) to mass spectrometry (MS) [1–10] have extended its versatility for a range of chemical [11–17], physical [18–23], and biomolecular structural studies [24–33]. Still relatively new to the biomedical field, several groups have recently begun to incorporate LC-IMS-MS workflows in proteomics studies [34–37], and enhanced performance has been demonstrated [38]. Given the recent rate of growth in the IMS

field [39] and its broad analytical utility, it seems prudent to expect that full maturity—both in terms of application workflows and technology performance—is yet to come.

On a microscopic scale in a drift tube, the kinetic energy ions gain in the electric field is dampened by individual collision events that collectively generate a steady-state drag force. A key feature is that the drag force, qv_d/K , along the length of the drift region is constant, allowing for a description of the ion motion based upon a measurable macroscopic drift velocity, v_d [40],

$$v_d = KE \quad (1)$$

where q is elemental charge, K is the ion mobility coefficient, and E is the electric field.

Conceptually, trapped ion mobility spectrometry (TIMS) represents the inversion of the conventional IMS experiment. That is, unlike drift tube IMS where ions are constantly pushed through a stationary gas by an electric field, TIMS utilizes an electric field to hold ions stationary against a moving gas. A

Electronic supplementary material The online version of this article (doi:10.1007/s13361-015-1310-z) contains supplementary material, which is available to authorized users.

Correspondence to: Melvin A. Park; e-mail: melvin.park@bruker.com

comprehensive description of TIMS principles is provided in references [41–43]. As the name suggests, during the course of TIMS analysis, ions are initially trapped and then eluted over time according to their mobility. The action of a gas stream pushes ions towards an outlet against a counteracting force from a DC electric field. After a user-selected accumulation time, additional ions are prevented from entering the analyzer while the trapped ions are eluted by decreasing the electric field over time. Because the force on the ions due to the gas stream depends on the mobility of the ions, the lowest mobility ions are forced out of the analyzer against the electric field first, while higher mobility ions elute later.

Recently, we derived a first-principles theory for TIMS that clarifies the dependence of analyzer performance on instrument properties, user-defined experimental parameters, and ion characteristics [43]. The resolving power (R) equation for TIMS ultimately reduces to an expression identical to the result Hill et al. arrived at for drift tube IMS [44],

$$R = \sqrt{\frac{qLE}{16 \ln 2 k_b T}} \quad (2)$$

providing a sensible check of the derivation. In Equation 2, k_b is Boltzmann's constant, and T is the temperature. In drift tube IMS, the path length, L , is simply equivalent to the physical length of the tube. However, in the alternative IMS technique termed, "parallel flow IMS," gas flows in a direction opposite that of ion motion, effectively increasing the path length of the ions [45]. The effective path length in parallel flow IMS becomes the sum of a physical length of the analyzer and the product of gas velocity and ion transit time [45]. Similarly, under the approximation that the effective path length is greater than the physical dimensions of the analyzer ($v_g t_p \gg L_p$), TIMS resolving power can be written as,

$$R = \sqrt{\frac{qv_g t_p E_e}{16 \ln 2 k_b T}} \quad (3)$$

where t_p is the transit time across the electric field gradient (EFG) plateau, and E_e is the electric field on the plateau at the time of elution. Thus, in Equation 3, the product $v_g t_p$ represents the effective drift length. Knowing that

$$E_e = v_g / K \quad (4)$$

$$t_p = \sqrt{\frac{2L_p}{K\beta}} \quad (5)$$

where L_p is the length of the EFG plateau and β is the electric field scan rate, it is possible to rearrange

Equation 3 to yield an expression where TIMS resolving power is described by the key separation parameters,

$$R = v_g \cdot \sqrt[4]{\frac{2L_p}{\beta}} \cdot \frac{1}{\sqrt[4]{K^3}} \cdot \sqrt{\frac{q}{16 \ln 2 k_b T}} \quad (6)$$

In agreement with theory, experimental conditions that increase the work done on the ions—i.e., high pressures that increase v_g and reduce K , as well as slow EFG scans that reduce β —result in increased resolving power. Experimentally, TIMS resolving powers have exceeded 200 for singly charged ions [42, 43] and approached 300 for multiply charged ions [46, 47]. Previous experimental measurements have confirmed the dependence of resolving power on β and K ; however, the dependence of resolving power on flow parameters has not yet been fully explored [43].

Here, the gas flow is studied by computational fluid dynamics (CFD) simulations and ion mobility experiments. Notice from Equation 3, the analytically useful work done (i.e., $qE_e v_g t_p$) occurs as ions traverse the plateau. Thus, the gas dynamics in the vicinity of the plateau are of particular interest. By characterizing the flow in this region, we seek to (1) quantify the magnitude of v_g , (2) experimentally validate the theoretical dependence of the flow parameters on R , and (3) expand the original theory to include spatial dependence of the flow variables.

Experimental

Instrumentation

A list of key terms and variables used to describe TIMS instrumentation is provided in the Appendix. A TIMS funnel was incorporated into the first vacuum stage of a prototype ESI-QqTOF (Bruker Daltonics, Billerica, MA, USA) mass spectrometer. A diagram of the TIMS funnel and the vacuum

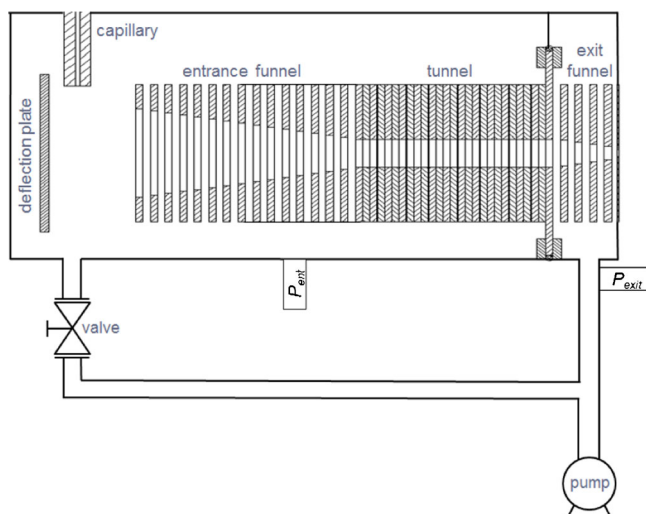


Figure 1. Cutaway view of the TIMS apparatus and vacuum configuration

configuration used to generate variable gas flow through the tunnel is shown in Figure 1. Analyte ions were produced by electrospray ionization (ESI) at atmospheric pressure. Ions entrained in nitrogen gas pass through a glass capillary into the first pumping region of the instrument. Importantly, the bore of the capillary is orthogonal to the axis of the TIMS funnel (see Figure 1). Thus, the flow of gas introduced through the capillary into the first pumping chamber is directed toward the pumping port, rather than down the length of the tunnel. Ions are deflected orthogonally out of the gas stream and into the entrance funnel by applying a repulsive potential to the deflection plate.

The TIMS analyzer is comprised of three regions: the entrance funnel, tunnel, and exit funnel. The analysis sequence includes an “accumulation step” wherein ions from the source are stored in the tunnel and an “elution step” wherein stored ions are released according to their mobility. During the accumulation step, the potential on the deflection plate is set such that ions are transmitted into the entrance funnel and, subsequently, the tunnel. During the elution step, the potential on the deflection plate is set to prevent additional ions from entering the tunnel. The length and diameter of the tunnel are 46 mm and 8 mm, respectively. The resistor values inside the tunnel are set such that the EFG increases linearly from the entrance to an axial position approximately midway down the tunnel whereupon the electric field becomes constant (see Figure 4).

The difference in pressure across the tunnel, ΔP , is varied by restricting the flow of gas through the valve positioned opposite the capillary exit. In the present work, the entrance and exit funnel regions are pumped using a two-stage rotary vane vacuum pump (Alcatel, 2033 SD, 39 m³/h; Hingham, MA, USA). The magnitude of the gas velocity was determined at the position of ion elution ($z = 23.3$ mm, see Figure 4) using the signal at m/z 922 contained in ESI tuning mix ($P_3N_3(OCH_3CF_2CF_2)_6 [M + H]^+$, $K_0 = 0.828$ cm² V⁻¹ s⁻¹, Agilent Technologies, Santa Clara, CA, USA). In these experiments, the sample was infused into the pneumatic sprayer of the ESI source at ~ 180 μ L/h. Previous datasets revealed that the gas velocities calculated were not strongly dependent on the ion species used (i.e., 160 ± 1 m/s at 2.9 mbar and 180 ± 2 m/s at 3.1 mbar for m/z 622 to 1822) [43]. Thus, in this work, we selected m/z 922 because this particular ion is trapped with good efficiency at the operational rf frequency of ~ 870 kHz and amplitude of ~ 200 V_{*p-p*}. The DC field strength required to trap m/z 922 at the operational pressures (details provided below) is approximated to be between 49 and 68 Td at the elution position. The dependence of resolving power on drag force was validated using a range of tuning mix ions m/z 622 to 1522.

The DC voltage in the TIMS analyzer is defined via an RC network that spans the tunnel and includes inputs at either end. During the elution step, the magnitude of the DC potential on the front of the tunnel (and therefore across the RC network) is decreased over time. The resistor values between plates in the tunnel are tunable potentiometers, the value of which can be set to within 1% of the desired value. The circuit is designed such that the RC time constant is small with respect to the separation timescale. The measured elution time is related to the DC potential on the front of the tunnel via its initial value and the

scan rate. In the present study, this potential changes linearly with time at a fixed rate. The electric field strength along the tunnel axis (see Figure 4) was calculated based on the values of the resistors in the RC network, the potentials at the inputs of the network, and the electrode geometry in the TIMS analyzer using SIMION 8.1 (Ringoos, NJ, USA).

CFD Simulations

Detailed properties related to the local pressure, temperature, and flow velocity inside the tunnel were modeled using Comsol Multiphysics 5.0. The effect of including high Mach number flow physics and slip wall boundaries was initially examined; best agreement between simulation and experiment was obtained using the single-phase laminar flow user module that solves the Navier-Stokes equations for conservation of momentum, and the continuity equation for conservation of mass [48].

$$\rho(\mathbf{v} \cdot \nabla) \mathbf{v} = \nabla \cdot \left[-P\mathbf{I} + \mu(\nabla \mathbf{v} + (\nabla \mathbf{v})^T) - \frac{2}{3} \mu(\nabla \cdot \mathbf{v})\mathbf{I} \right] + \mathbf{F} \quad (7)$$

$$\nabla \cdot (\rho \mathbf{v}) = 0 \quad (8)$$

where ρ is the fluid density, μ is the dynamic viscosity, \mathbf{v} is the flow velocity, P is the pressure, T is the temperature, and \mathbf{F} represents body forces. In the case of non-isothermal flow, heat transfer from the thermal walls to the fluid was also considered. This approach yielded a total of $\sim 2.7 \cdot 10^6$ domain elements and a solution in ~ 30 min using a computer equipped with 8 GB RAM and a 2.7 GHz core i5-3340 M processor (Intel, Santa Clara, CA, USA).

Treatment of the gas as a continuous fluid requires that the ratio of the mean free path (λ) be significantly smaller than the characteristic flow dimension. This ratio, known as the Knudsen number (Kn), is valid so long as $\text{Kn} < 0.01$ [48]. Considering the flow occurs through the cylindrical tunnel at an average operational pressure of ~ 3 mbar and ambient temperature, the mean free path is expected to be ~ 20 μ m yielding $\text{Kn} \sim 0.002$. The approach is further justified by estimating the gas velocity through the analyzer on the basis of mass flow. Considering the tunnel conductance, pumping speed, and pressure, the flow velocity is estimated to be less than 150 m/s at the tunnel entrance—i.e., well within the subsonic range.

Flow through the tunnel was simulated considering the simplified physical geometry of the analyzer and the measured local pressure in the regions bracketing the tunnel. Experimentally, the pressures in the entrance funnel (2.7 mbar $\leq P_{ent} \leq 3.4$ mbar) and at the exit funnel pumping port ($P_{exit} = 1.6$ mbar in all cases) were determined using Pirani gauges used to track changes within ± 0.1 mbar (Pfeiffer Vacuum, TPR 270; Asslar, Germany). The measured pressures were used as inlet and outlet constraints in the simulations. The boundary condition for the entrance funnel pressure was set outside the sealed entrance funnel whereas the boundary

condition for the exit funnel was set by the pressure measured on a pumping port located ~ 90 mm from the vacuum chamber. Turbulent forces were not included in the simulations because the estimated Reynolds number ($Re \sim 150$) is well below the limit ($Re \sim 2000$) where non-laminar behavior is expected.

Secondary effects from adjacent regions of the instrument (i.e., the free jet expansion at the ESI gas/ion inlet and flow into the vacuum chamber downstream of the exit funnel) were not considered in the present model. As mentioned above, the directed gas flow at the capillary exit is orthogonal to the axis of the TIMS funnel and, therefore, is expected to have only a small effect. Furthermore, based on the dimensions of the capillary, the Mach disk should occur within ~ 7 mm of the capillary exit, which is small in comparison to the length of the entrance funnel (~ 50 mm). Based on conductance, gas flow through the aperture at the end of the exit funnel is expected to be $<10\%$ of the total flow through the exit funnel during TIMS operation.

Results and Discussion

Gas Flow Characterization

TIMS analysis begins by accumulating ions for a user-selected period of time, typically on the order of a few tens of milliseconds. Ions enter the analyzer and are trapped at an equilibrium position along the EFG rising edge corresponding to their mobility coefficient. When the magnitude of the EFG is decreased from its initial value, ions begin to move toward the plateau. Elution occurs when the field strength on the plateau, E_e , is such that the drift velocity of the ions, given by Equation 4, is equal and opposite the velocity of the gas through the tunnel,

$$v_d + v_g = 0 \quad (9)$$

Thus, if K is known and E_e is measured, Equation 4 provides a means for determining v_g .

Gas flow is generated through the tunnel by restricting flow through the port across from the capillary exit (Figure 1). Restricting the conductance at this port increases the pressure difference across, and the mass flow through, the tunnel. To determine the gas velocity, the field strength at the EFG plateau at the time of elution, E_e , for an ion of interest must be known. However, what is actually measured is the time at which the ion arrives at the TOF detector. This time is related to instantaneous field strength at which the ion is detected, E_t . Note that E_t and E_e differ slightly because in a TIMS-qTOF instrument, the ions require time to travel from the TIMS analyzer to the TOF analyzer. A convenient means to determine E_e is thus achieved by simply scanning the EFG relatively slowly such that E_t has not decreased significantly during ion transit from the exit of the TIMS analyzer to the detector. Considering the electric field scan rate (β) of $7084 \text{ V m}^{-1} \text{ s}^{-1}$ for the data shown in Figure 2 and a post-TIMS transit time of ~ 5 ms, the absolute magnitude

of E_t is less than E_e by only 35 V m^{-1} translating into $\leq 1\%$ error.

Figure 2a shows the change in E_e as a function of gas pressure in the entrance funnel, P_{ent} . As the entrance funnel pressure is increased (and therefore the pressure difference across the tunnel is increased), ions are pushed further up the repulsive EFG rising edge such that the electric field at elution increases. Figure 2b shows that the increase in E_e is due to both a decrease in K and an increase in v_g . That is, if we assume that P_{ent} is representative of the pressure at the point of ion elution and E_e is the electric field strength at the time of elution, then dividing E_e by P_{ent} will yield a value proportional to gas velocity because $E_e = v_g/K$, and K is inversely proportional to P_{ent} . Because we can expect the pressure drop across the tunnel to be linearly related to P_{ent} (i.e., $\Delta P = P_{ent} - P_{exit}$), and that the subsonic gas velocity in a tube will be proportional to the pressure drop across the tube, we can also expect v_g to be proportional to P_{ent} . Thus, in Figure 2b, we observed that, as expected, the gas velocity (E_e/P_{ent}) is a linear function of P_{ent} and therefore, the pressure across the tunnel.

A reasonable estimation of the gas velocity through the tunnel can be made using the elution field strengths shown in Figure 2 and Equation 4, assuming the flow is isothermal and that the entrance funnel pressure is equivalent to the local pressure at the elution position. On the basis of these assumptions, the results shown in Table 1 confirm that (1) consistent with the initial flow estimate, the velocity of the gas is in the subsonic regime, and (2) as previously noted, the velocity of the gas increases proportionally to the pressure difference across the tunnel. However, because this approximation does not account for gas expansion, we can expect this approach to provide an estimate of the gas velocity that is lower than the actual velocity at the elution position. That is, gas expansion in the tunnel would cause a decrease in pressure and an increase in the gas velocity along the tunnel axis. As shown below, accounting for gas expansion provides a more accurate representation of the fluid dynamics at work in TIMS.

To gain a more detailed insight into the flow dynamics in the tunnel, CFD simulations were performed. As shown in Figure 3, the flow fields were first simulated for the experimental conditions where the measured pressure difference across the tunnel was minimal ($P_{ent} = 2.7$ mbar). These conditions are highlighted because any potential effects caused downstream by the free jet expansion at the capillary exit should be minimized when the pumping port in line with the capillary is partially open. The simulations indicate that the local pressure at the tunnel entrance is slightly less than the pressure in the entrance funnel chamber by ~ 0.1 mbar. In addition, a small pressure gradient of ~ 0.3 mbar is generated across the tunnel region itself (Figure 3d) leading to a concomitant nonlinear increase in v_g along the tunnel axis (Figure 3c). When the fluid is treated as non-isothermal, a near identical pressure profile is observed along with similar qualitative trends, though the slightly lower gas velocity is accompanied by a decrease in temperature of a few degrees Kelvin (Figure 3e). It is perhaps worthwhile to point out that the

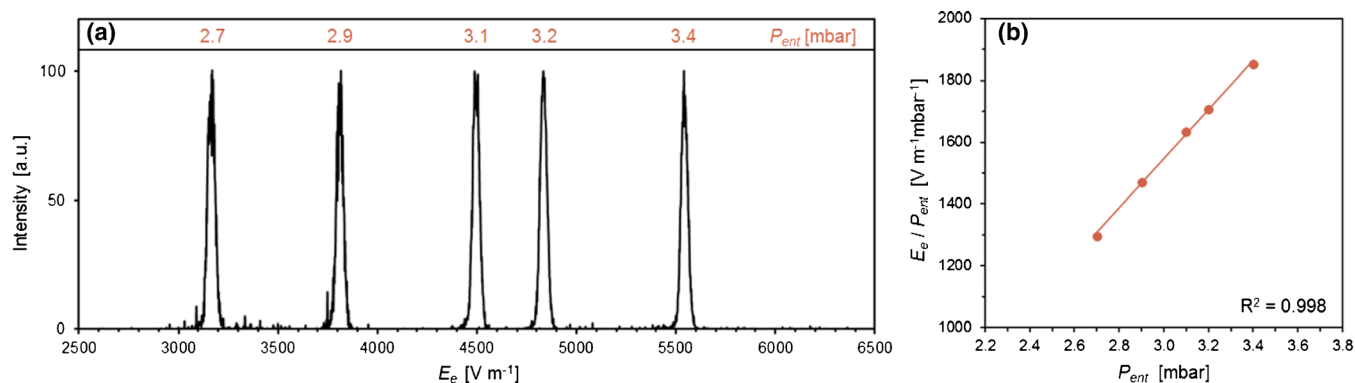


Figure 2. (a) Mass-selected TIMS distributions of m/z 922 obtained at fixed $\beta = 7084 \text{ V} \cdot \text{m}^{-1} \text{s}^{-1}$ and varied pressure in the entrance funnel, as labeled above. In (b), E_e/P_{ent} is plotted against P_{ent} showing the pressure-dependent contribution of v_g

electrode structures in the TIMS tunnel are segmented into four quadrants for the purpose of generating a quadrupolar rf field. The gaps between the four quadrants along the length of the analyzer break the otherwise cylindrical symmetry of the tunnel. However, the CFD results shown in Figure 3f suggest that though the radial flow profile near the electrode surfaces differs from that along the gaps, the flow profile contained in the cylindrical volume occupied by ions ($r \sim \pm 1$ mm) remains highly symmetric.

Using the local pressure and temperature determined by CFD simulations at the position of elution and the method described above, the gas velocity acting upon the ions was recalculated using Equation 4 for both isothermal and non-isothermal treatment of the gas. In Table 2, similar to the discussion with respect to Figure 2, K_{expt} was calculated from the known reduced mobility constant as well as the local pressure, P_e , and temperature, T_e , at the elution position given by simulation. The electric field strength at the time of elution, E_e , was experimentally measured. The experimental gas velocity, $v_{g,expt}$, was calculated based on K_{expt} and E_e and compared with the gas velocity determined from simulation, $v_{g,e}$. The results, shown in Table 2, indicate excellent agreement at $P_{ent} = 2.7$ mbar between experiment and simulations for both approaches. In both cases, the error between simulation and experiment is $<1\%$. The results also indicate that temperature effects are expected to be relatively minor since comparatively, non-isothermal and isothermal treatment of the gas yields velocities that differ only by 3 m/s (see Figure 3c). To confirm the relatively small effect of temperature, a resistive temperature sensor was placed approximately midway down the tunnel and the gas temperature was measured as the flow through the

tunnel was varied over the range of pressures listed in Table 2. Though a minor effect, the gas temperature was found to be 2 K lower when the valve across from the capillary was set to a closed position (i.e., higher v_g) as opposed to an open position. Because the Knudsen number is relatively low and a small temperature drop was experimentally observed, the non-isothermal model is expected to be slightly more accurate and was used henceforth.

Across the range of pressures investigated, good quantitative agreement between the v_g values obtained using the non-isothermal simulation model and experiment is observed at pressures below 3 mbar ($\leq 4\%$ error), whereas reasonable agreement is observed at higher pressures (8% to 13% error). Likely sources of error include (1) perturbations in the tunnel flow due to the capillary inflow when pumping is restricted in the entrance funnel, (2) error in the gauge pressures measured, (3) simplification of the vacuum system for flow simulations on a reasonable timescale required for prototyping, (4) the exact position of ion elution due to curvature of the electric field at the elution position (see Figure 4), and (5) compressibility effects as the flow approaches Ma 0.3.

It is also noteworthy that the present TIMS model accounts only for ion motion in the z -dimension. Accordingly, the magnitude of the flow discussed is along the central separation axis ($r = 0$). While good agreement is observed between simulation and experiment, experimentally, a swarm of ions experiences the radial average of a developing (quasi)-parabolic flow profile. Based on the simulations shown in Figure 3f, ions confined within $r \pm 1$ mm experience an average flow that may differ by up to 4%. While a small decrease in resolving power is expected on this basis, experimental evidence does not suggest that ions of higher m/z (having weaker pseudopotential confinement) experience an effectively lower gas velocity (see the Experimental section). That the magnitude of the gas velocity does not indicate an m/z dependence suggests that under typical operating conditions where charge repulsion effects are small, all ions sample a similar average velocity distribution and/or the methodology used herein is not sufficiently sensitive to detect this subtle trend.

More important than exact quantitative agreement between simulation and experiment is that all results indicate that

Table 1. Gas Velocity Values Calculated Using Equation 4 and the Approximation that the Pressure at the Elution Position is Equivalent to the Entrance Funnel Pressure

P_{ent} [mbar]	K [$\text{m}^2 \cdot \text{V}^{-1} \text{s}^{-1}$]	E_e [$\text{V} \cdot \text{m}^{-1}$]	$v_{g,expt}$ [$\text{m} \cdot \text{s}^{-1}$]
2.7	0.0341	3165	108
2.9	0.0318	3811	121
3.1	0.0297	4495	134
3.2	0.0288	4834	139
3.4	0.0271	5542	150

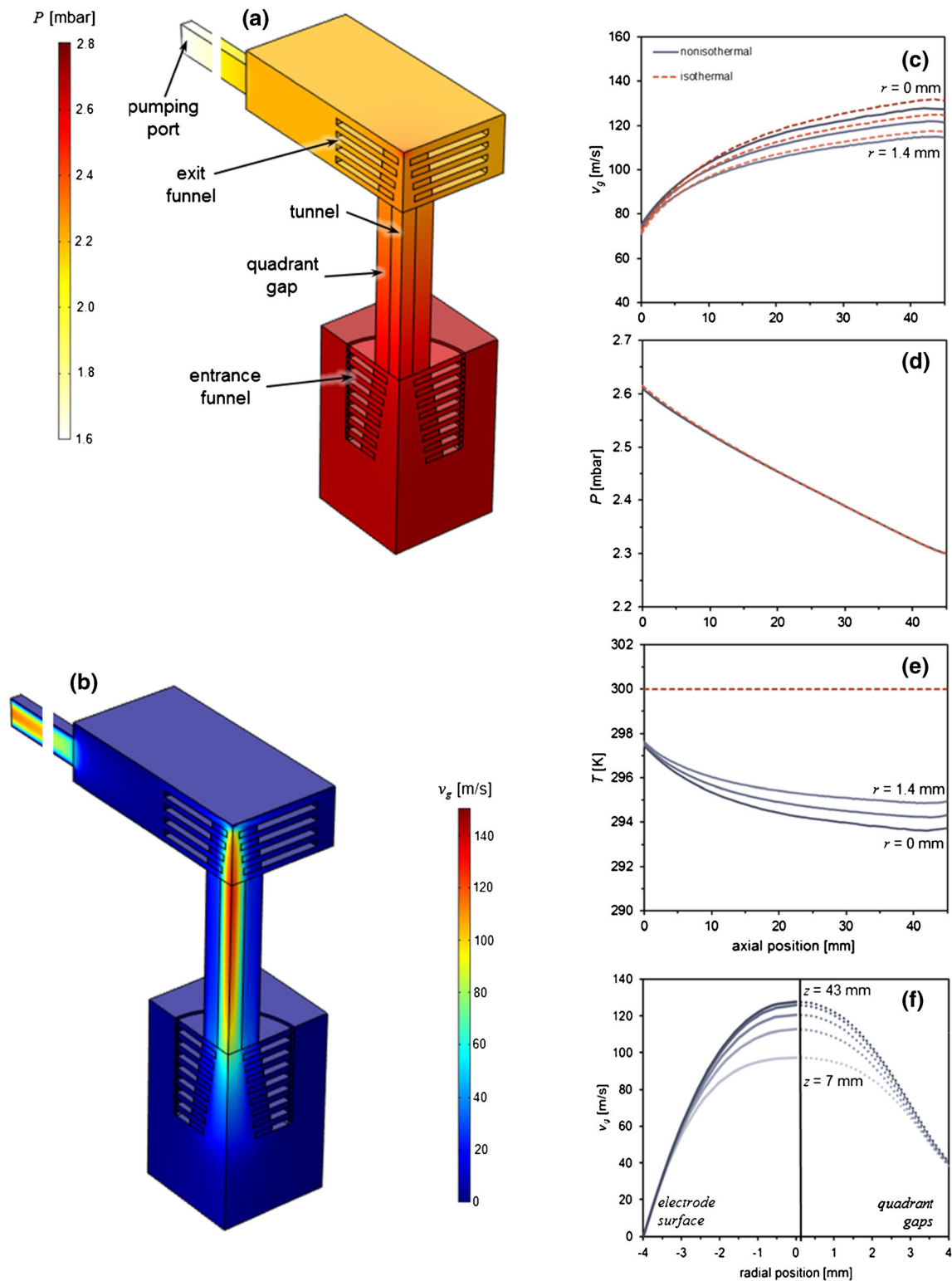


Figure 3. Three-dimensional cutaway view of (a) the simulated pressure and (b) the gas velocity through the tunnel considering non-isothermal fluid flow. The right panel contains plots of (c) the gas velocity, (d) pressure, and (e) temperature in the tunnel extracted at $r = 0, 1,$ and 1.4 mm. For comparison, results from isothermal treatment of the gas are also shown (red dashed line). In panel (f), the radial flow profile obtained from non-isothermal treatment of the gas is shown at axial positions of 7, 17, 27, 37, and 43 mm. The solid line represents the gas profile from the center of the tunnel to the electrode surface, whereas the dotted line represents the profile from the center to the gaps between electrode quadrants

Table 2. Comparison of (non-)Isothermal CDF Simulations and Experimental Results. Experimental Gas Velocity Values Were Determined Using the Local Pressure and Temperature at the Elution Position from Simulations to Solve Equation 4

P_{ent} [mbar]	P_e [mbar]	T_e [K]	K_{expt} [m ² ·V ⁻¹ ·s ⁻¹]	E_e [V·m ⁻¹]	CFD $v_{g,e}$ [m·s ⁻¹]	TIMS $v_{g,expt}$ [m·s ⁻¹]
2.7	2.4	300 [†]	0.0379	3165	121	120
2.7	2.4	294	0.0372	3165	118	118
2.9	2.6	293	0.0348	3811	128	133
3.1	2.7	292	0.0328	4495	136	147
3.2	2.8	292	0.0318	4834	139	154
3.4	3.0	291	0.0301	5542	144	167

[†] Indicates isothermal flow conditions.

increasing the pressure difference across the tunnel results in a proportional increase in the magnitude of the gas flow. It is also useful to consider the relative change in the gas velocity resulting from a change in pressure. As shown in Figure 2b, plotting E_e/P_{ent} versus P_{ent} removes the dependence of E on P (or rather, the dependence E on K) and allows for an independent assessment of the relative change in field strength at elution that results from changing v_g . That E_e/P_{ent} increases from 11.72 to 16.30 Vcm⁻¹mbar⁻¹ as a result of increasing the pressure from 2.7 to 3.4 mbar indicates that the magnitude of the velocity acting on the ions increases by the same factor (28%) by Equation 4. Consistent with this experimental data, the $v_{g,e}$ values independently obtained from CFD simulations (see Table 2) also predict that the flow velocity increases by 22% as the result of the increase in ΔP .

Drag Force

From theory, the total transit time (t_t) through the TIMS tunnel, neglecting gas expansion effects, is given by [43],

$$t_t = \frac{E_0 - v_g/K}{\beta} + \sqrt{\frac{2L_p}{K\beta}} + \ln\left(\frac{v_g}{\sqrt{2K\beta}L_p}\right) \cdot \frac{L_f}{v_g - \sqrt{2K\beta}L_p} \quad (10)$$

where E_0 is the initial electric field strength on the plateau and L_f is the length of the EFG falling edge. The first term in

Equation 10 is the difference in time from the start of the experiment to the time ions begin to elute. The second term is the time for ions to cross the EFG plateau. The third term, the time for ions to traverse the EFG falling edge near the exit of the analyzer, is negligible and is not discussed further here.

Of principal interest is the fluid dynamics along the EFG plateau, since Equation 3 indicates that a majority of the analytically useful work is done in this region. Results thus far indicate that an increase in v_g is accompanied by a decrease in pressure, resulting in an increase in K , though the original TIMS model based on Equation 10 treated these variables as constants. If, instead, K is treated as a function of position, the transit time across the plateau from Equation 5 becomes

$$t_p = \sqrt{\frac{2L_p}{K(L_r)\beta}} \sqrt{\frac{\log(\epsilon + 1)}{\epsilon}} \quad (11)$$

where

$$\epsilon = \Delta K / K(L_r) \quad (12)$$

and L_r is the length of the rising edge. Note that a complete derivation of TIMS theory considering position-dependent flow variables is presented in the [Supporting Information](#). Results presented in Figure 3 indicate that the change in mobility across the EFG

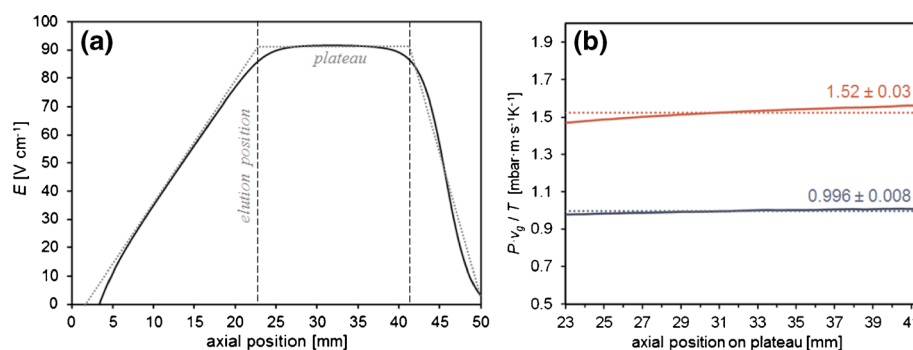


Figure 4. (a) EFG profile generated at fixed radial position ($r = 0$) with 305 V across the tunnel. (b) Drag force, represented by the term $v_g P/T$, plotted along EFG plateau at an entrance funnel pressure of 2.7 mbar (blue) and 3.4 mbar (red). The solid line represents the solution obtained by CFD simulations, whereas the dotted line represents the average

plateau, ΔK , is reasonably small ($\lesssim 5\%$) such that $[\log(\epsilon + 1)/\epsilon]^{1/2} > 0.988$. Furthermore, in the limit,

$$\lim_{\epsilon \rightarrow 0} \sqrt{\frac{\log(\epsilon + 1)}{\epsilon}} = 1 \quad (13)$$

Equation 11 simplifies to the original expression given in Equation 5.

A similar discussion and derivation can be extended to the TIMS resolving power expression (Equation 3); however, for the sake of brevity the reader is directed to the [Supporting Information](#) for additional details. Here, it suffices to mention that the spatial dependence of the variables associated with the flow can be accounted for in terms of ϵ , and that as ϵ approaches zero, the original TIMS resolving power expression (Equations 3 and 6) is returned.

As we discussed previously [35], the transit time across the plateau is typically much shorter than the elution time, meaning that the total time described in Equation 10 further simplifies to the first term,

$$t_e = \frac{E_0 - \frac{v_g}{K}}{\beta} \quad (14)$$

Equation 14 indicates that the elution time is not dependent on the spatial variation of v_g or K but, instead, depends only on the instantaneous gas velocity and mobility at the elution position. This outcome supports previous calibration of the analyzer wherein the field strength at elution is linearly related to the reduced mobility coefficient.

Nonetheless, it is interesting to consider the idea of drag force as it relates to gas expansion and the variation of gas temperature, pressure, and velocity. The drag force here is given by $F_d = qE = qv_g/K$. Substituting $K_0P_0T/(PT_0)$ for K in Equation 14 gives

$$t_e = \frac{E_0 - \left(\frac{v_g P T_0}{T P_0 K_0}\right)}{\beta} \quad (15)$$

where the explicit drag force is equal to

$$F_d = \frac{q v_g P T_0}{T P_0 K_0} \quad (16)$$

In a TIMS experiment, the terms E_0 , $T_0/(P_0K_0)$, and β in Equation 15 are constants, whereas the previous findings presented herein indicate that v_g , P , and T each slightly varies as a function of position. However, Figure 4b demonstrates that in the current operational flow regime, an increase in v_g is indeed largely balanced by a decrease in P and a small decrease in T . That is, the simulations show that the collective change in the drag force across the plateau is small ($\lesssim 3\%$) and can be

neglected. Thus, the drag force on the ions during separation across the EFG plateau in TIMS is position-independent.

In drift tube IMS, drag force is constant along the entire length of the tube. Clearly, it is possible to express the resolving power expression for drift tube IMS in terms of the drag force—i.e., simply substitute $F_d = qv_d/K$ for qE in Equation 2. The TIMS resolving power expression may be rewritten similarly by substitution of Equation 16 into Equation 3,

$$R = \sqrt{\frac{qv_g P T_0}{T P_0 K_0}} \cdot \sqrt{\frac{v_g t_p}{16 \ln 2 k_b T}} \quad (17)$$

Next, by substituting Equation 5 into Equation 17 and rearranging we obtain

$$R = F_d \cdot \sqrt{\frac{1}{q 16 \ln 2 k_b T}} \cdot \sqrt[4]{\frac{2KL_p}{\beta}} \quad (18)$$

Consistent with Equation 6, a fourth root dependence on L_p/β and a square root dependence on T is apparent. The $\sqrt[4]{\frac{1}{K^3}}$ and \sqrt{q} dependences from Equation 6 are present, but not obvious because of the consolidation of terms in F_d .

Equation 18 indicates that the resolving power is directly proportional to F_d . To validate this dependence, the experimental resolving power was plotted as a function of F_d for tuning mix ions at each of the five pressure conditions described in Tables 1 and 2. The data contained in Figure 5a indicate that in agreement with the theoretical dependence of F_d on R , the resolving power is indeed proportional to the magnitude of the drag force. The data also indicate that a small mobility dependence, observed as a sub-trend, is present. Figure 5b shows that when the additional dependence of K —present in the form of a fourth-root term that is not contained in F_d —is considered, the correlation strengthens and the experimental trends more closely match those predicted by Equation 18. It is likely that the residual sub-trend observed in Figure 5b is attributed to the assumption that $\epsilon \rightarrow 0$ across the plateau. Simulations indicate that this assumption is valid within $\sim 3\%$ and the experimentally observed dependence is of a similar magnitude.

It should be noted that while variations in K and v_g are now accounted for in the revised derivation, spatial variations in the diffusion coefficient, D , across the EFG plateau could not be successfully incorporated, but may be considered in future work. Nevertheless, the collective work supports the notion that TIMS theory can reasonably predict the resolving power trends observed by experiment.

Finally, it is interesting to consider the implications of increasing the drag force, for example, by doubling the gas velocity while keeping all other variables in Equation 16 constant. While different flow physics may be required for accurately matching CFD simulations with experiments that employ higher Mach number flow, the gas flow should remain

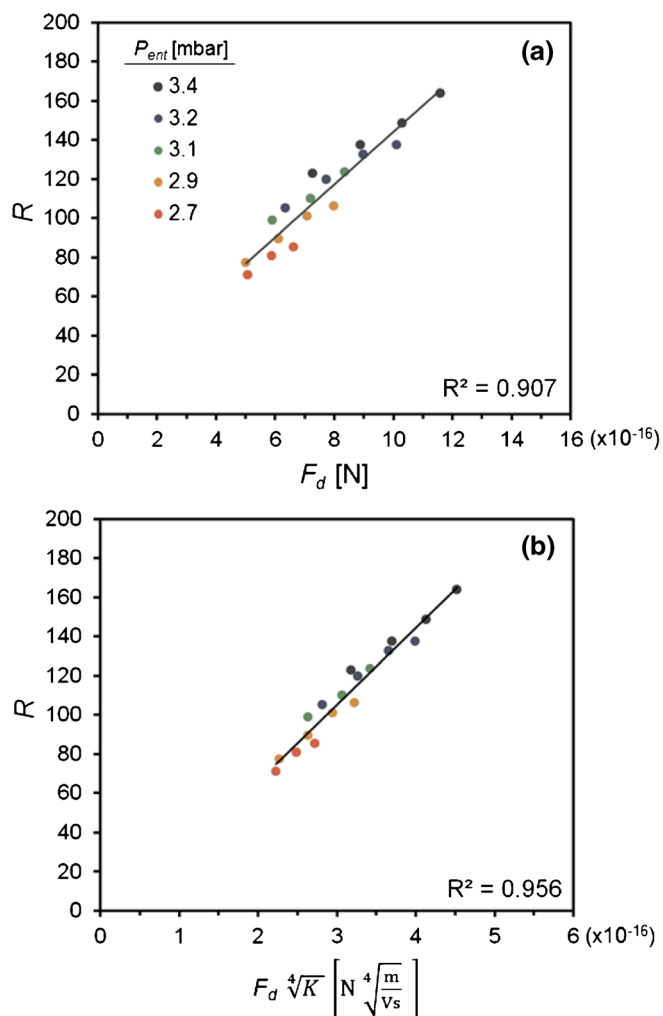


Figure 5. Experimental resolving power trend as a function of (a) F_d and (b) $F_d \cdot \sqrt[4]{K}$ for data acquired at the five different pressures listed in Tables 1 and 2

subsonic. Extrapolation of the experimental data contained in Figure 5b indicates a resolving power of 300 could be achieved for singly charged ions. Given that resolving powers between ~ 250 and 300 have already been experimentally attained for peptide and protein ions with the existing TIMS apparatus [46, 47], it seems reasonable to expect even better performance for multiply charged ions, such as those encountered in proteomics applications [49].

Conclusions

The gas velocity, pressure gradient, and flow profile in TIMS have been characterized using simulations and ion mobility experiments. The results indicate that a relatively small pressure gradient (~ 0.3 mbar) along the separation axis induces a high, but subsonic, flow velocity toward the analyzer exit. Laminar fluid flow develops along the tunnel axis, with v_g values ranging between ~ 120 and 170 m/s at the position of

ion elution, depending on the pressure difference across the tunnel.

As noted previously, the majority of the analytically useful work is done on the ions as they traverse the EFG plateau. Thus, the gas dynamics on the plateau are of particular interest. The increase in v_g along the separation axis—especially in the vicinity of the plateau—is largely balanced by an increase in K (due to the decrease in P and increase in T) leading to a near-constant drag force acting upon the ions in the tunnel. Thus, analogous to drift tube IMS, the drag force on the ions in TIMS is nearly constant where the analytically useful work is done. This near constancy in drag force ($< 2\%$ variation) and related variables greatly simplify the level of theory required and allows for use of the relatively simple, previously derived equations to describe TIMS behavior. Nonetheless, we derive a more comprehensive model, which accounts for the spatial dependence of these variables. As one might expect, the newly derived equations reduce to the previously derived equations as the spatial dependence of v_g and K become negligible. In agreement with simulations, experimental resolving power trends were found to be in close agreement with the theoretical dependence of the drag force assuming that spatial dependence of the flow variables is small, thus validating another principal component of the theory. Both theory and experimental results indicate that further resolving power improvement can be expected by increasing the drag force on the ions.

Appendix

List of Key Terms and Variables

EFG	electric field gradient; the complete EFG profile includes the rising edge, plateau, and falling edge
elution position	axial position in the tunnel where ions begin to elute across the plateau; in this work, the elution position is located at $z = 23.3$ mm and is defined by the resistor values and the geometry of the plates in the tunnel
E_e	strength of the EFG plateau at the time of ion elution
E_t	strength of the EFG plateau at the time of ion detection
K_{expt}	mobility coefficient at the elution position determined by experiment
P_e	local pressure in the tunnel at the elution position determined by simulation
P_{ent}	measured pressure in the entrance funnel
P_{exit}	measured pressure in the exit funnel
ΔP	pressure difference across the tunnel
t_e	time elapsed from the start of the EFG scan ($t = 0$) to the time when ions begin to elute across the plateau
t_p	time elapsed during ion transit across the EFG plateau
v_g	velocity of the buffer gas through the tunnel

$v_{g, \text{expt}}$	experimentally measured velocity of the buffer gas measured at the elution position
$v_{g, e}$	velocity of the buffer gas at the elution position determined by simulation
E_e	instantaneous electric field across the tunnel at the time of ion elution
E_t	instantaneous electric field across the tunnel when ions are detected
β	rate at which the strength of the field on the EFG plateau (E_p) is scanned

References

- Shaffer, S.A., Tang, K., Anderson, G.A., Prior, D.C., Udseth, H.R., Smith, R.D.: A novel ion funnel for focusing ions at elevated pressure using electrospray ionization mass spectrometry. *Rapid Commun. Mass Spectrom.* **11**, 1813–1817 (1997)
- Gillig, K.J., Ruotolo, B., Stone, E.G., Russell, D.H., Fuhrer, K., Gonin, M., Schultz, A.J.: Coupling high-pressure MALDI with ion mobility/orthogonal time-of-flight mass spectrometry. *Anal. Chem.* **72**, 3965–3971 (2000)
- Giles, K., Pringle, S.D., Worthington, K.R., Little, D., Wildgoose, J.L., Bateman, R.H.: Applications of a traveling wave-based radio-frequency-only stacked ring ion guide. *Rapid Commun. Mass Spectrom.* **18**, 2401–2414 (2004)
- Koeniger, S.L., Merenbloom, S.I., Valentine, S.J., Jarrold, M.F., Udseth, H.R., Smith, R.D., Clemmer, D.E.: An IMS-IMS analogue of MS-MS. *Anal. Chem.* **78**, 4161–4174 (2006)
- Baker, E.S., Clowers, B.H., Li, F., Tang, K., Tolmachev, A.V., Prior, D.C., Belov, M.E., Smith, R.D.: Ion mobility spectrometry-mass spectrometry performance using electrodynamic ion funnels and elevated drift gas pressures. *J. Am. Soc. Mass Spectrom.* **18**, 1176–1187 (2007)
- Clowers, B.H., Ibrahim, Y.M., Prior, D.C., Danielson, W.F., Belov, M.E., Smith, R.D.: Enhanced ion utilization efficiency using an electrodynamic ion funnel trap as an injection mechanism for ion mobility spectrometry. *Anal. Chem.* **80**, 612–623 (2008)
- Kemper, P.R., Dupuis, N.F., Bowers, M.T.: A new, higher resolution ion mobility mass spectrometer. *Int. J. Mass Spectrom.* **287**, 46–57 (2009)
- Glaskin, R.S., Ewing, M.A., Clemmer, D.E.: Ion trapping for ion mobility spectrometry measurements in a cyclical drift tube. *Anal. Chem.* **85**, 7003–7008 (2013)
- May, J.C., Goodwin, C.R., Lareau, N.M., Leaprot, K.L., Morris, C.B., Kurulugama, R.T., Mordehai, A., Klein, C., Barry, W., Darland, E., Overney, G., Imatani, K., Stafford, G.C., Fjeldsted, J.C., McLean, J.A.: Conformational ordering of biomolecules in the gas phase: nitrogen collision cross sections measured on a prototype high resolution drift tube ion mobility-mass spectrometer. *Anal. Chem.* **86**, 2107–2116 (2014)
- Webb, I.K., Garimella, S.V.B., Tolmachev, A.V., Chen, T.C., Zhang, X., Norheim, R.V., Prost, S.A., LaMarche, B., Anderson, G.A., Ibrahim, Y.M.: Experimental evaluation and optimization of structures for lossless ion manipulations for ion mobility spectrometry with time-of-flight mass spectrometry. *Anal. Chem.* **86**, 9169–9176 (2014)
- Gidden, J., Bowers, M., Jackson, A., Scrivens, J.: Gas-phase conformations of cationized poly(styrene) oligomers. *J. Am. Soc. Mass Spectrom.* **13**, 499–505 (2002)
- Steiner, W.E., Harden, C.S., Hong, F., Klopsch, S.J., Hill Jr., H.H., McHugh, V.M.: Detection of aqueous phase chemical warfare agent degradation products by negative mode ion mobility time-of-flight mass spectrometry [IM(TOF)MS]. *J. Am. Soc. Mass Spectrom.* **17**, 241–245 (2006)
- Trimpin, S., Clemmer, D.E.: Ion mobility spectrometry/mass spectrometry snapshots for assessing the molecular compositions of complex polymeric systems. *Anal. Chem.* **80**, 9073–9083 (2008)
- Brocker, E.R., Anderson, S.E., Northrop, B.H., Stang, P.J., Bowers, M.T.: Structures of metallosupramolecular coordination assemblies can be obtained by ion mobility spectrometry-mass spectrometry. *J. Am. Chem. Soc.* **132**, 13486–13494 (2010)
- Schenk, E.R., Mendez, V., Landrum, J.T., Ridgeway, M.E., Park, M.A., Fernandez-Lima, F.: Direct observation of differences of carotenoid polyene chain cis/trans isomers resulting from structural topology. *Anal. Chem.* **86**, 2019–2024 (2014)
- Benigni, P., Thompson, C.J., Ridgeway, M.E., Park, M.A., Fernandez-Lima, F.: Targeted high-resolution ion mobility separation coupled to ultrahigh-resolution mass spectrometry of endocrine disruptors in complex mixtures. *Anal. Chem.* **87**, 4321–4325 (2015)
- McKenzie-Coe, A., DeBord, J.D., Ridgeway, M., Park, M., Eiceman, G., Fernandez-Lima, F.: Lifetimes and stabilities of familiar explosive molecular adduct complexes during ion mobility measurements. *Analyst* **140**, 5692–5699 (2015)
- von Helden, G., Gotts, N.G., Bowers, M.T.: Experimental evidence for the formation of fullerenes by collisional heating of carbon rings in the gas phase. *Nature* **363**, 60–63 (1993)
- Wytenbach, T., von Helden, G., Batka, J., Carlat, D., Bowers, M.T.: Effect of the long-range potential on ion mobility measurements. *J. Am. Soc. Mass Spectrom.* **8**, 275–282 (1997)
- May, J.C., Russell, D.H.: A mass-selective variable-temperature drift tube ion mobility-mass spectrometer for temperature dependent ion mobility studies. *J. Am. Soc. Mass Spectrom.* **22**, 1134–1145 (2011)
- Servage, K.A., Silveira, J.A., Fort, K.L., Russell, D.H.: Evolution of hydrogen bond networks in protonated water clusters $H^+(H_2O)_n$ ($n = 1$ to 120) studied by cryogenic ion mobility-mass spectrometry. *J. Phys. Chem. Lett.* **11**, 1825–1830 (2014)
- Fernandez-Lima, F.A., Becker, C., Gillig, K., Russell, W.K., Nascimento, M.A.C., Russell, D.H.: Experimental and theoretical studies of $(Cs)_nCs^+$ cluster ions produced by 355 nm laser desorption ionization. *J. Phys. Chem. A* **112**, 11061–11066 (2008)
- Servage, K.A., Fort, K.L., Silveira, J.A., Shi, L., Clemmer, D.E., Russell, D.H.: Unfolding of hydrated alkyl diammonium cations revealed by cryogenic ion mobility-mass spectrometry. *J. Am. Chem. Soc.* **137**, 8916–8919 (2015)
- Ruotolo, B.T., Benesch, J.L.P., Sandercock, A.M., Hyung, S.J., Robinson, C.V.: Ion mobility-mass spectrometry analysis of large protein complexes. *Nat. Protoc.* **3**, 1139–1152 (2008)
- Utrecht, C., Barbu, I.M., Shoemaker, G.K., van Duijn, E., Heck, A.J.R.: Interrogating viral capsid assembly with ion mobility-mass spectrometry. *Nat. Chem.* **3**, 126–132 (2011)
- Bleiholder, C., Dupuis, N.F., Wytenbach, T., Bowers, M.T.: Ion mobility-mass spectrometry reveals a conformational conversion from random assembly to B-sheet in amyloid fibril formation. *Nat. Chem.* **3**, 172–177 (2011)
- Wytenbach, T., Bowers, M.T.: Structural stability from solution to the gas phase: native solution structure of ubiquitin survives analysis in a solvent-free ion mobility-mass spectrometry environment. *J. Phys. Chem. B* **115**, 12266–12275 (2011)
- Hall, Z., Politis, A., Bush, M.F., Smith, L.J., Robinson, C.V.: Charge-state dependent compaction and dissociation of protein complexes: insights from ion mobility and molecular dynamics. *J. Am. Chem. Soc.* **134**, 3429–3438 (2012)
- Silveira, J.A., Fort, K.L., Kim, D., Servage, K.A., Pierson, N.A., Clemmer, D.E., Russell, D.H.: From solution to the gas phase: stepwise dehydration and kinetic trapping of Substance P reveals the origin of peptide conformations. *J. Am. Chem. Soc.* **135**, 19147–19153 (2013)
- Chen, L., Chen, S.H., Russell, D.H.: An experimental study of the solvent-dependent self-assembly/disassembly and conformer preferences of gramicidin A. *Anal. Chem.* **85**, 7826–7833 (2013)
- Shi, L., Holliday, A.E., Shi, H., Zhu, F., Ewing, M.A., Russell, D.H., Clemmer, D.E.: Characterizing intermediates along the transition from polyproline I to polyproline II using ion mobility spectrometry-mass spectrometry. *J. Am. Chem. Soc.* **136**, 12702–12711 (2014)
- Masson, A., Kamrath, M., Perez, M., Glover, M., Rothlisberger, U., Clemmer, D., Rizzo, T.: Infrared spectroscopy of mobility-selected H⁺-Gly-Pro-Gly-Gly (GPGG). *J. Am. Soc. Mass Spectrom.* **26**, 1444–1454 (2015)
- Glover, M.S., Bellinger, E.P., Radivojac, P., Clemmer, D.E.: Penultimate proline in neuropeptides. *Anal. Chem.* **87**, 8466–8472 (2015)
- Tenzer, S., Moro, A., Kuharev, J., Francis, A.C., Vidalino, L., Provenzani, A., Macchi, P.: Proteome-wide characterization of the RNA-binding protein RALY-interactome using the in vivo-biotinylation-pulldown-quant (iBioPQ) approach. *J. Proteome Res.* **12**, 2869–2884 (2013)
- Parviainen, V., Joenvaara, S., Tohmola, N., Renkonen, R.: Label-free mass spectrometry proteome quantification of human embryonic kidney cells following 24 hours of sialic acid overproduction. *Proteome Sci.* **11**, 38 (2013)
- Dator, R.P., Gaston, K.W., Limbach, P.A.: Multiple enzymatic digestions and ion mobility separation improve quantification of bacterial ribosomal proteins by data independent acquisition liquid chromatography-mass spectrometry. *Anal. Chem.* **86**, 4264–4270 (2014)

37. Helm, S., Dobritzsch, D., Rodiger, A., Agne, B., Baginsky, S.: Protein identification and quantification by data-independent acquisition and multi-parallel collision-induced dissociation mass spectrometry (MSE) in the chloroplast stroma proteome. *J. Proteome* **98**, 79–89 (2014)
38. Helm, D., Vissers, J.P.C., Hughes, C.J., Hahne, H., Ruprecht, B., Pachi, F., Grzyb, A., Richardson, K., Wildgoose, J., Maier, S. K.: Ion mobility tandem mass spectrometry enhances performance of bottom-up proteomics. *Mol. Cell. Proteom.* **13**, 3709–3715 (2014)
39. May, J.C., McLean, J.A.: Ion mobility-mass spectrometry: time-dispersive instrumentation. *Anal. Chem.* **87**, 1422–1436 (2015)
40. Mason, E.A., McDaniel, E.W.: *Transport Properties of Ions in Gases*. John Wiley and Sons, New York (1988)
41. Park, M.A.: Apparatus and method for parallel flow ion mobility spectrometry combined with mass spectrometry. US Patent 7,838,826 (2010)
42. Hernandez, D.R., DeBord, J.D., Ridgeway, M.E., Kaplan, D.A., Park, M.A., Fernandez-Lima, F.: Ion dynamics in a trapped ion mobility spectrometer. *Analyst* **139**, 1913–1921 (2014)
43. Michelmann, K., Silveira, J., Ridgeway, M., Park, M.: Fundamentals of trapped ion mobility spectrometry. *J. Am. Soc. Mass Spectrom.* **26**, 14–24 (2015)
44. Rokushika, S., Hatano, H., Baim, M., Hill, H.H.: Resolution measurement for ion mobility spectrometry. *Anal. Chem.* **57**, 1902–1907 (1985)
45. Tammet, H.: The limits of air ion mobility resolution. Proceedings of the 11th International Conference on Atmospheric Electricity; NASA, MSFC, Alabama, June 7–11, 1999, pp. 626–629 (1999)
46. Silveira, J.A., Ridgeway, M.E., Park, M.A.: High resolution trapped ion mobility spectrometry of peptides. *Anal. Chem.* **86**, 5624–5627 (2014)
47. Ridgeway, M.E., Silveira, J.A., Meier, J.E., Park, M.A.: Microheterogeneity within conformational states of ubiquitin revealed by high resolution trapped ion mobility spectrometry. *Analyst* **140**, 6964–6972 (2015)
48. Comsol Multiphysics, CFD User's Guide, Version 4.3b (2015)
49. Beck, S., Michalski, A., Raether, O., Lubeck, M., Kaspar, S., Goedecke, N., Baessmann, C., Hornburg, D., Meier, F., Paron, I.: The impact II, a very high resolution quadrupole time-of-flight instrument for deep shotgun proteomics. *Mol. Cell. Proteomics.* **14**, 2014–2029 (2015)